

# Statistically Steady Turbulence in Soap Films: Direct Numerical Simulations with Ekman Friction

Prasad Perlekar<sup>1,\*</sup> and Rahul Pandit<sup>1,†</sup>

<sup>1</sup>*Centre for Condensed Matter Theory, Department of Physics,  
Indian Institute of Science, Bangalore 560012, India.*

We present a detailed direct numerical simulation (DNS) designed to investigate the combined effects of walls and Ekman friction on turbulence in forced soap films. We concentrate on the forward-cascade regime and show how to extract the isotropic parts of velocity and vorticity structure functions and thence the ratios of multiscaling exponents. We find that velocity structure functions display simple scaling whereas their vorticity counterparts show multiscaling; and the probability distribution function of the Weiss parameter  $\Lambda$ , which distinguishes between regions with centers and saddles, is in quantitative agreement with experiments.

PACS numbers: 47.27.ek, 47.27.Gs, 47.27.Jv

The pioneering work of Kraichnan [1] showed that fluid turbulence in two dimensions (2D) is qualitatively different from that in three dimensions (3D): in the former we have an infinity of extra conserved quantities, in the inviscid, unforced case; the first of these is the enstrophy. It turns out, therefore, that 2D turbulence displays an inverse cascade of energy, from the length scale at which the force acts to larger length scales, and a forward cascade of enstrophy, from the forcing length scale to smaller ones; by contrast, 3D turbulence is characterised by a forward cascade of energy [2]. Kraichnan's predictions were first confirmed in atmospheric experiments in quasi-two-dimensional, stratified flows [3]; subsequent experiments have studied systems ranging from large-scale geophysical flows to soap films [3, 4, 5, 6, 7, 8]. The latter have proved to be especially useful in characterizing 2D turbulence.

We present the first direct numerical study (DNS) that has been designed specifically to explore the combined effects of the air-drag induced Ekman friction  $\alpha$  and walls on the forward cascade in 2D turbulence; and we employ the Kolmogorov forcing used in many soap-film experiments [5, 6, 7, 8]. Thus we can make a far more detailed comparison with these experiments than has been attempted hitherto. In particular, if we use values of  $\alpha$  that are comparable to those in experiments, we find that the energy dissipation rate because of the Ekman friction is comparable to the energy dissipation rate that arises from the conventional viscosity. We show how to extract the isotropic parts [9] of velocity and vorticity structure functions and then, by using the extended self-similarity (ESS) procedure [10], we obtain ratios of multiscaling exponents whence we conclude that velocity structure functions show simple scaling whereas their vorticity counterparts display multiscaling. Most important, our probability distribution function (PDF) of the Weiss parameter  $\Lambda$  [11] is in quantitative agreement with that found in experiments [6, 7].

For the low-Mach-number flows we consider, we can

use the following soap-film equations [5, 12]:

$$(\partial_t + \mathbf{u} \cdot \nabla)\omega = \nu \nabla^2 \omega - \alpha \omega + F_\omega / \rho; \quad \nabla^2 \psi = \omega. \quad (1)$$

Here  $\mathbf{u} \equiv (-\partial_y \psi, \partial_x \psi)$ ,  $\psi$ , and  $\omega \equiv \nabla \times \mathbf{u}$  are, respectively, the velocity, stream function, and vorticity at the position  $\mathbf{x}$  and time  $t$ ; we choose the uniform density  $\rho = 1$ ;  $\alpha$  is the Ekman friction coefficient,  $\nu$  is the kinematic viscosity, and  $F_\omega \equiv k_{inj} F_0 \cos(k_{inj} x)$ , a Kolmogorov-type forcing term, with amplitude  $F_0$ , and injection wave vector  $k_{inj}$  (the length scale  $\ell_{inj} \equiv 2\pi/k_{inj}$ ). We impose no-slip ( $\psi = 0$ ) and no-penetration ( $\nabla \psi \cdot \hat{n} = 0$ ) boundary conditions on the walls, where  $\hat{n}$  is the outward normal to the wall. If we non-dimensionalize  $\mathbf{x}$  by  $k_{inj}^{-1}$ ,  $t$  by  $k_{inj}^{-2}/\nu$ , and  $F_\omega$  by  $2\pi/(k_{inj} \|F_\omega\|_2)$ , with  $\|F_\omega\|_2 \equiv (\int_A |F_\omega|^2 d\mathbf{x})^{1/2}$ , then we have two control parameters, namely, the Grashof [13] number  $\mathcal{G} = 2\pi \|F_\omega\|_2 / (k_{inj}^3 \rho \nu^2)$  and the non-dimensionalized Ekman friction  $\gamma = \alpha / (k_{inj}^2 \nu)$ . For a given set of values of  $\mathcal{G}$  and  $\gamma$ , the system attains a nonequilibrium statistical steady state after a time  $t/\tau \simeq 2.8$ , where  $\tau = L/u_{rms}$  is the box-size time,  $L$  the side of our square simulation domain, and  $u_{rms}$  the root-mean-square velocity. In this state the Reynolds number  $Re \equiv u_{rms}/(k_{inj} \nu)$ , the energy, etc., fluctuate; their mean values, along with one-standard-deviation error bars, are given in Table I that lists the values of the parameters in our runs R1–7.

We use a fourth-order Runge-Kutta scheme with step size  $\delta t = 10^{-4}$  for time marching in Eq. (1) and evaluate spatial derivatives via second-order and fourth-order, centered, finite differences, respectively, for points adjacent to the walls and for points inside the domain. The Poisson equation in (1) is solved by using a fast-Poisson solver [14] and  $\omega$  is calculated at the boundaries by using Thom's formula [15]. To evaluate spatiotemporal averages, we store  $\psi(\mathbf{x}, t_n)$  and  $\omega(\mathbf{x}, t_n)$ , with  $t_n = (4 + n\Delta)\tau$ ,  $n = 0, 1, 2, \dots, n_{max}$ , and  $96 \leq n_{max} \leq 200$ ;  $\Delta = 0.28$  for runs R1–6 and  $\Delta = 0.13$  for run R7.

Figures 1(a)-(f) show the time evolution of the kinetic energy  $E(t) \equiv (\int_A \mathbf{u}^2 d\mathbf{x})/A$ , viscous energy-dissipation

	$N$	$\alpha$	$F_0$	$\gamma$	$\mathcal{G}(\times 10^4)$	$Re$	$E$	$\epsilon_\nu$	$\epsilon_e$	$\tilde{\Lambda}(\times 10^2)$	$b$	$\delta_b(\times 10^{-2})$
R1	1025	0.45	45	0.25	3.5	$23.3 \pm 0.4$	$15.1 \pm 0.5$	$-28 \pm 2$	$-13.6 \pm 0.5$	$5.3 \pm 0.3$	$0.32 \pm 0.01$	$3.1 \pm 0.1$
R2	1025	1.25	45	0.71	3.5	$19.6 \pm 0.3$	$10.7 \pm 0.3$	$-28 \pm 1$	$-26.8 \pm 0.9$	$4.8 \pm 0.2$	$0.33 \pm 0.01$	$3.1 \pm 0.1$
R3	1025	1.25	60	0.71	4.7	$24.0 \pm 0.5$	$15.9 \pm 0.6$	$-40 \pm 2$	$-39.9 \pm 1.4$	$7.2 \pm 0.4$	$0.33 \pm 0.01$	$2.8 \pm 0.1$
R4	2049	0.45	45	0.25	3.5	$23.2 \pm 0.4$	$15.1 \pm 0.5$	$-28 \pm 2$	$-13.6 \pm 0.4$	$5.3 \pm 0.3$	$0.31 \pm 0.01$	$3.2 \pm 0.2$
R5	2049	1.25	45	0.71	3.5	$19.6 \pm 0.4$	$10.8 \pm 0.4$	$-28 \pm 1$	$-27.0 \pm 1.0$	$4.8 \pm 0.2$	$0.33 \pm 0.01$	$3.1 \pm 0.1$
R6	2049	1.25	60	0.71	4.7	$23.8 \pm 0.4$	$15.9 \pm 0.6$	$-40 \pm 2$	$-40.0 \pm 1.5$	$7.2 \pm 0.4$	$0.33 \pm 0.01$	$3.1 \pm 0.1$
R7	3073	0.45	45	0.25	3.0	$26.5 \pm 0.4$	$20.0 \pm 1.0$	$-26 \pm 2$	$-17.8 \pm 0.6$	$5.0 \pm 0.4$	$0.31 \pm 0.01$	$3.7 \pm 0.3$

TABLE I: Parameters for our runs R1-7:  $N$ , the number of grid points along each direction,  $\gamma$ ,  $\mathcal{G}$ ,  $Re$  (we use  $\nu = 0.016$ ,  $\ell_{inj} = 0.6$ , and a square simulation domain with side  $L = 7$ , grid spacing  $\delta_x = L/N$ , area  $A$ , and boundary  $\partial A$ ), the time-averaged kinetic energy, viscous-energy-dissipation rate, and the energy-dissipation rate because of Ekman friction,  $E$ ,  $\epsilon_\nu$ , and  $\epsilon_e$ , respectively,  $\tilde{\Lambda} \equiv \sqrt{\langle (\partial_x u_y')^2 \rangle \langle (\partial_y u_x')^2 \rangle}$ ,  $b \equiv -\langle \partial_x u_y' \partial_y u_x' \rangle / \tilde{\Lambda}$ , and the boundary-layer thickness  $\delta_b \propto \langle (\oint_{\partial A} \omega^2 / \oint_{\partial A} ((\nabla \omega) \cdot \hat{n})^2)^{1/2} \rangle$  [16].

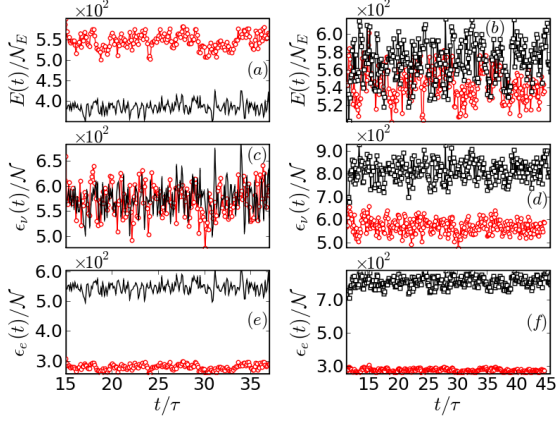


FIG. 1: (Color online) Representative plots from runs R1 (red circles), R2 (black lines), and R3 (black squares), showing the time evolution of  $E(t)/N_E$  [(a) and (b)],  $\epsilon_\nu(t)/N$  [(c) and (d)], and  $\epsilon_e(t)/N$  [(e) and (f)]. In (a), (c), and (e) we keep  $\mathcal{G}$  fixed and vary  $\gamma$  ( $\gamma = 0.25$  (red circles) and  $\gamma = 0.71$  (black line)). In (b), (d), and (f) we maintain  $Re \simeq 21.2$  by varying  $\gamma$  ( $\gamma = 0.25$  (red circles) and  $\gamma = 0.71$  (black squares)) and  $\mathcal{G}$ .

rate  $\epsilon_\nu(t) \equiv -\nu(\int_{\mathbf{A}} |\omega|^2 d\mathbf{x})/A$ , and energy-dissipation rate because of the Ekman friction  $\epsilon_e(t) = -2\alpha E(t)$  (non-dimensionalized, respectively, by  $N_E \equiv (\nu k_{inj})^2$  and  $N \equiv -k_{inj}^4 \nu^3$ ). The mean values  $E \equiv \langle E(t) \rangle$ ,  $\epsilon_\nu \equiv \langle \epsilon_\nu(t) \rangle$ , and  $\epsilon_e \equiv \langle \epsilon_e(t) \rangle$ , given in Table I, are comparable to those in experiments; note that  $\epsilon_\nu$  and  $\epsilon_e$  are of similar magnitudes. By comparing data from runs R1 (red circles) and R2 (black lines) in Figs. 1(a), (c), and (e) we see that, if we fix  $\mathcal{G}$  and increase  $\gamma$ ,  $E$  decreases,  $\epsilon_\nu$  remains unchanged (within error bars), and  $\epsilon_e$  increases. If we change both  $\mathcal{G}$  and  $\gamma$ , we can keep the mean  $Re$  fixed, as in runs R1 and R3 in Table I, by compensating an increase in  $\gamma$  with an increase in  $\mathcal{G}$  (cf. Ref. [6]); in Figs. 1(b), (d), and (f) we see, by comparing runs R1 (red circles) and R3 (black squares), that  $E$  remains unchanged (within error bars), whereas both  $\epsilon_\nu$  and  $\epsilon_e$  increase as  $\gamma$  and  $\mathcal{G}$  increase in such a way that  $Re$  is held fixed.

Since Kolmogorov forcing is inhomogeneous, we use the decomposition  $\psi = \langle \psi \rangle + \psi'$  and  $\omega = \langle \omega \rangle +$

$\omega'$ , where the angular brackets denote a time average and the prime the fluctuating part [20], to calculate the order- $p$  velocity and vorticity structure functions  $S_p(\mathbf{r}_c, \mathbf{R}) \equiv \langle |(\mathbf{u}'(\mathbf{r}_c + \mathbf{R}) - \mathbf{u}'(\mathbf{r}_c)) \cdot \mathbf{R}/R|^p \rangle$  and  $S_p^\omega(\mathbf{r}_c, \mathbf{R}) \equiv \langle |\omega'(\mathbf{r}_c + \mathbf{R}) - \omega'(\mathbf{r}_c)|^p \rangle$ , respectively, where  $\mathbf{R}$  has magnitude  $R$  and  $\mathbf{r}_c$  is an origin. Figures 2(a) and (b) show pseudocolor plots of  $S_2(\mathbf{r}_c, \mathbf{R})$  and  $S_2^\omega(\mathbf{r}_c, \mathbf{R})$ , respectively, for  $\mathbf{r}_c = (2, 2)$ ; other values of  $\mathbf{r}_c$  yield similar results so long as they do not lie near the boundary layer (Table I) of thickness  $\delta_b$  ( $\mathbf{r}_c$  is chosen at least  $5\delta_b$  away from all boundaries). We now calculate  $S_2(\mathbf{R}) \equiv \langle S_2(\mathbf{r}_c, \mathbf{R}) \rangle_{\mathbf{r}_c}$  and  $S_2^\omega(\mathbf{R}) \equiv \langle S_2^\omega(\mathbf{r}_c, \mathbf{R}) \rangle_{\mathbf{r}_c}$ , where the subscript  $\mathbf{r}_c$  denotes an average over the origin (we use  $\mathbf{r}_c = (i, j)$ ,  $2 \leq i, j \leq 5$ ); these averaged structure functions [Figs. 2(c) and (d)] are nearly isotropic for  $R < \ell_{inj}$  but not so for  $R > \ell_{inj}$ . To obtain the isotropic parts in an  $SO(2)$  decomposition of these structure functions [9] we integrate over the angle  $\theta$  that  $\mathbf{R}$  makes with the  $x$  axis to obtain  $S_p(R) \equiv \int_0^{2\pi} S_p(\mathbf{R}) d\theta$  and  $S_p^\omega(R) \equiv \int_0^{2\pi} S_p^\omega(\mathbf{R}) d\theta$ . Given  $S_p(R)$  and  $S_p^\omega(R)$  we use the extended-self-similarity (ESS) procedure [10] to extract the multiscaling-exponent ratios  $\zeta_p/\zeta_2$  and  $\zeta_p^\omega/\zeta_2^\omega$ , respectively, from the slopes (in the forward-cascade inertial range) of log-log plots of  $S_p(r)$  versus  $S_2(r)$  [Fig. 2(e)] and  $S_p^\omega(R)$  versus  $S_2^\omega(R)$  [Fig. 2(f)] [21]. The insets Figs. 2(e1) and (f1) show, respectively, plots of the local slopes  $\chi_p \equiv d \log_{10} S_p(R) / d \log_{10} S_2(R)$  versus  $\log_{10} S_2(R)$  and  $\chi_p^\omega \equiv d \log_{10} S_p^\omega(R) / d \log_{10} S_2^\omega(R)$  versus  $\log_{10} S_2^\omega(R)$  in the forward-cascade regime; the mean values of  $\chi_p$  and  $\chi_p^\omega$ , over the ranges shown, yield the exponent ratios  $\zeta_p/\zeta_2$  and  $\zeta_p^\omega/\zeta_2^\omega$  that are plotted versus  $p$  in Figs. 2 (e2) and (f2), respectively, in which the error bars indicate the maximum deviations of  $\chi_p$  and  $\chi_p^\omega$  from their mean values. The Kraichnan-Leith-Batchelor (KLB) predictions [1] for these exponent ratios, namely,  $\zeta_p^{KLB}/\zeta_2^{KLB} \sim r^{p/2}$  and  $\zeta_p^{\omega, KLB}/\zeta_2^{\omega, KLB} \sim r^0$ , agree with our values for  $\zeta_p/\zeta_2$  but not  $\zeta_p^\omega/\zeta_2^\omega$ : velocity structure functions do not display multiscaling [Fig. 2 (e2)] whereas their vorticity analogs do [note the curvature of the plot in Fig. 2 (f2)]. This is in consonance with the results of DNS studies with periodic boundary

conditions [17, 18]. Indeed, if we use the same values of  $\gamma$  as in Ref. [17], we obtain the same exponent ratios (within error bars); thus our method for the extraction of the isotropic parts of the structure functions suppresses boundary and anisotropy effects efficiently.

For an inviscid, incompressible 2D fluid the local flow topology can be characterized via the Weiss criterion [11] that uses the invariant  $\Lambda \equiv (\omega^2 - \sigma^2)/8$ , where  $\sigma^2 \equiv \sum_{i,j} \sigma_{ij} \sigma_{ji}$  and  $\sigma_{ij} \equiv (\partial_i u_j + \partial_j u_i)$ . This criterion provides a useful measure of flow properties even if  $\nu > 0$  as noted in the experiments of Ref. [6]: Regions with  $\Lambda > 0$  and  $\Lambda < 0$  correspond to centers and saddles as we show in Fig. 3 (a) by superimposing, at a representative time, a pseudocolor plot of  $\Lambda$  on contours of  $\psi$ . This result is in qualitative accord with experiments [see, e.g., Fig. 1 of Ref. [6] and also earlier DNS studies [11], which do not use Ekman friction]. In Fig. 3 (b) we compare the scaled PDFs  $P_2(\Lambda/\Lambda_{rms})$  with data obtained from points near the walls (black curve) and from points in the bulk (red curve); the clear difference between these, not highlighted before, indicates that regions of large  $\Lambda$  are suppressed in the boundary layers. There is a generation of strain and vorticity in these boundary layers and scatter plots, not shown, indicate  $\omega^2 \simeq \sigma^2$  here; this leads to the suppression of regions of large  $\Lambda$  in  $P_2(\Lambda/\Lambda_{rms})$ .

Figures 3 (c) and (d) show the PDF  $P_1(\Lambda)$  and the scaled PDF  $P_2(\Lambda/\Lambda_{rms})$  for runs R4 (red line) and R5 (blue dashed line), with  $\gamma = 0.25$  and  $\gamma = 0.71$ , respectively, and  $\mathcal{G} = 3.5 \times 10^4$ ; by comparing these figures we see that both  $P_1$  and  $P_2$  overlap within error bars for runs R4 and R5. We believe this is because, in fixed- $\mathcal{G}$  runs like R4 and R5,  $\epsilon_\nu$  does not change [Table I] even though  $\gamma$  changes. By contrast, if we compare  $P_1$  and  $P_2$  [Figs. 3 (e) and (f)] for runs R4 (red line) and R6 (blue dashed line), in which the mean  $Re$  is held fixed by tuning both  $\gamma$  and  $\mathcal{G}$ , we find, in agreement with experiments [6], that the PDFs  $P_1$  do not agree for these runs, but the PDFs  $P_2$  overlap within error bars. Our results for  $P_2$  in Fig. 3(f) are in quantitative agreement with experiments: we have obtained the points in this plot by digitising data points [see <http://www.frantz.fi/software/g3data.php>] in Fig. 2(d) of Ref. [6]; the errors in these points are comparable to the spread of data in [6]. Conditional expectation values of  $\langle \sigma^2 \rangle$  and  $\langle \omega^2 \rangle$ , for a given value of  $\Lambda$ , also agree well with experiments as can be seen by comparing Fig. 4 with Fig. 3 of Ref. [6]. We also present in Figs. 4 (b-d) pseudocolor plots of the joint PDFs of  $\delta\omega(r) \equiv \omega'(\mathbf{x} + r\hat{e}_x) - \omega'(\mathbf{x})$ ,  $\delta u_L(r) \equiv u'_x(\mathbf{x} + r\hat{e}_x) - u'_x(\mathbf{x})$  or  $\delta u_T(r) \equiv u'_y(\mathbf{x} + r\hat{e}_x) - u'_y(\mathbf{x})$  with  $\Lambda' \equiv \det(M)$ ,  $M^{\alpha\beta} \equiv \int_\Omega m^{\alpha\beta} d\mathbf{r} / \int_\Omega d\mathbf{r}$ ,  $m^{\alpha\beta} \equiv \partial_\alpha u'_\beta$ ,  $\Omega$  a circular disc with center at  $\mathbf{x} + (r/2)\hat{e}_x$  and radius  $r/2$ , and  $r$  in the forward-cascade regime; we obtain striking agreement with experiments as can be seen by comparing Figs. 4 (c-d) with Figs. 1-2 of Ref. [7]. Finally, we calculate  $\tilde{\Lambda} \equiv \sqrt{\langle (\partial_x u'_y)^2 \rangle \langle (\partial_y u'_x)^2 \rangle}$  and  $b \equiv -\langle \partial_x u'_y \partial_y u'_x \rangle / \tilde{\Lambda}$  (see

Table I) and obtain excellent agreement with experiments [6].

Some earlier numerical studies of 2D, wall-bounded, statistically steady turbulent flows [16] use forcing functions that are not of the Kolmogorov type; furthermore, they do not include Ekman friction. Other numerical studies, which include Ekman friction and Kolmogorov forcing, employ periodic boundary conditions [17, 18, 19]. To the best of our knowledge our study of 2D *turbulent* flows is the first one that accounts for Ekman friction, realistic boundary conditions, and Kolmogorov forcing. Thus we can make quantitative comparisons with soap-film experiments; and the agreement between our results and those of Refs. [5, 6, 7, 8] vindicates the use Eq. (1) as a model for these soap films [12]. We hope our results will stimulate experimental studies designed to extract (a) the isotropic parts of structure functions (and thereby to probe the multiscaling of vorticity structure functions [Fig. 2 (f1)]) or (b) the PDF  $P_2(\Lambda/\Lambda_{rms})$  [Fig. 3 (b)] near soap-film boundaries.

We thank J. Bec, G. Falkovich, V. Kumar, D. Mitra, and S.S. Ray for discussions, CSIR, DST, and UGC(India) for financial support, and SERC(IISc) for computational facilities. RP is a member of the International Collaboration for Turbulence Research.

---

\* Electronic address: perlekar@physics.iisc.ernet.in

† Electronic address: rahul@physics.iisc.ernet.in; also at Jawaharlal Nehru Centre For Advanced Scientific Research, Jakkur, Bangalore, India

- [1] R. Kraichnan, Phys. Fluids **10**, 1417 (1967); C. Leith, Phys. Fluids, **11**, 671 (1968); G. Batchelor, Phys. Fluids Suppl. II **12**, 233 (1969).
- [2] U. Frisch, *Turbulence the legacy of A.N. Kolmogorov* (Cambridge University Press, Cambridge, 1996).
- [3] G. Boer and T. Shepherd, J. Atmos. Sci. **40**, 164 (1983).
- [4] S. Danilov and D. Gurarie, Phys.-Usp. **43**, 863 (2000); H. Kellay and W. Goldburg, Rep. Prog. Phys. **65**, 845 (2002); P. Tabeling, Phys. Rep. **362**, 1 (2002).
- [5] M. Rivera and X.L. Wu, Phy. Rev. Lett. **85**, 976 (2000).
- [6] M. Rivera, X.L. Wu, and C. Yeung, Phys. Rev. Lett. **87**, 044501 (2001).
- [7] W.B. Daniel and M.A. Rutgers, Phys. Rev. Lett. **89**, 134502 (2002).
- [8] M. Rivera and R. Ecke, arXiv:0710.5888v1 (2007).
- [9] E. Bouchbinder, I. Procaccia, and S. Sela, Phys. Rev. Lett. **95**, 255503 (2005).
- [10] R. Benzi *et al.*, Phys. Rev. E **48**, R29 (1993).
- [11] J. Weiss, Physica D **48**, 273 (1992); A. Provenzale and A. Babiano, J. Fluid Mech. **257**, 533 (1993).
- [12] J. Chomaz, J. Fluid Mech. **442**, 387 (2001).
- [13] C. Doering and J. Gibbon, pp. 23-24, *Applied Analysis of the Navier-Stokes equations* (Cambridge University Press, Cambridge, 1995).
- [14] W. Press, B. Flannery, S. Teukolsky, and W. Vetterling, pp. 848-852, *Numerical Recipes in Fortran* (Cambridge University Press, Cambridge, 1992).



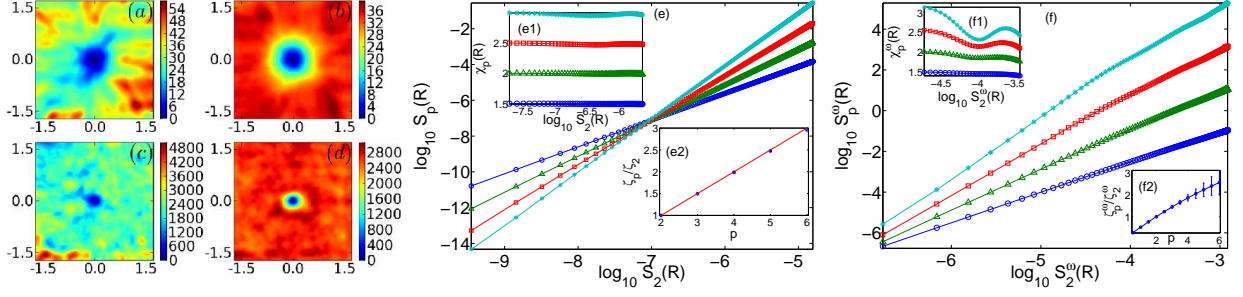


FIG. 2: (Color online) Pseudocolor plots of (a)  $S_2(\mathbf{r}_c, \mathbf{R})$ , for  $\mathbf{r}_c = (2, 2)$ , (b)  $S_2(R)$  (average of  $S_2(\mathbf{r}_c, \mathbf{R})$  over  $\mathbf{r}_c$ ), (c)  $S_2^\omega(\mathbf{r}_c, \mathbf{R})$ , for  $\mathbf{r}_c = (2, 2)$ , and (d)  $S_2^\omega(R)$  (average of  $S_2^\omega(\mathbf{r}_c, \mathbf{R})$  over  $\mathbf{r}_c$ ). Log-log ESS plots of the isotropic parts of the order- $p$  (e) velocity structure functions  $S_p(R)$  versus  $S_2(R)$  and (f) the vorticity structure functions  $S_p^\omega(R)$  versus  $S_2^\omega(R)$ ;  $p = 3$  (blue line with circles),  $p = 4$  (green line with triangles),  $p = 5$  (red line with squares), and  $p = 6$  (cyan line with stars); plots of the local slopes  $\chi_p$  and  $\chi_p^\omega$  (see text), in the forward-cascade inertial range: (e1)  $\chi_p$  versus  $\log_{10} S_2(R)$  and (f1)  $\chi_p^\omega$  versus  $\log_{10} S_2^\omega(R)$ . Plots versus  $p$  of the exponent ratios (e2)  $\zeta_p/\zeta_2$ , along with the KLB prediction (red line), and (f2)  $\zeta_p^\omega/\zeta_2^\omega$  and error bars from the local slopes (see text). All plots are for run R7.

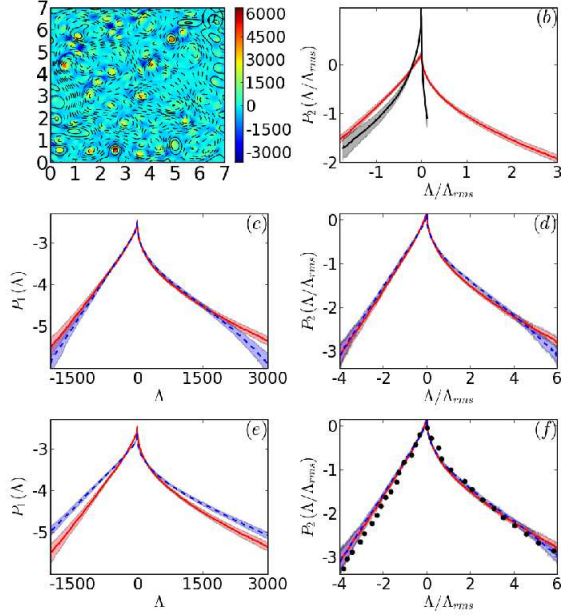


FIG. 3: (Color online) (a) Representative pseudocolor plot of  $\Lambda$  superimposed on a contour plot of the stream function  $\psi$ ; (b) the PDF  $P_1(\Lambda)$  obtained from points in the bulk  $\delta_b < x, y < L - \delta_b$  (red line) and from those points within a distance  $\delta_b$  from the boundaries (black line) for our run R7; plots of (c)  $P_1(\Lambda)$  versus  $\Lambda$  and (d)  $P_2(\Lambda/\Lambda_{rms})$  versus  $\Lambda/\Lambda_{rms}$  for fixed  $\mathcal{G}$  and  $\gamma = 0.25$  (red line) and  $\gamma = 0.71$  (blue dashed line) [runs R4 and R5]; plots of (e)  $P_1(\Lambda)$  versus  $\Lambda$  and (f)  $P_2(\Lambda/\Lambda_{rms})$  versus  $\Lambda/\Lambda_{rms}$  [runs R4 and R6 with  $Re \simeq 23.5$ ] and  $\gamma = 0.25$  (red line) and  $\gamma = 0.71$  (blue dashed line) and points (black dots) extracted from Fig. 2(d) of Ref. [6]. In (c)-(f) the fluctuating part of the velocity is used for  $\Lambda$ . One-standard-deviation error bars are indicated by the shaded regions.

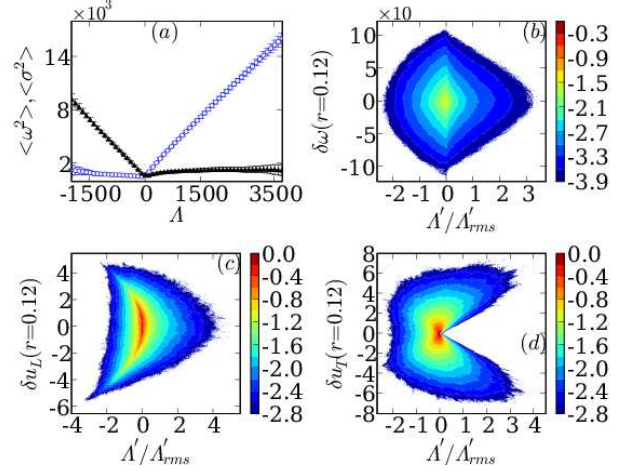


FIG. 4: (Color online) (a) Plots of conditional expectation values, with one-standard-deviation error bars, of  $\langle \sigma^2 \rangle$  (dots) and  $\langle \omega^2 \rangle$  (circles) for a given  $\Lambda$ ; pseudocolor plots of (b) the joint PDF  $P(\delta\omega(r = 0.12), \Lambda'/\Lambda'_{rms})$ , (c) the joint PDF  $P(\delta u_L(r = 0.12), \Lambda'/\Lambda'_{rms})$ , and (d) the joint PDF  $P(\delta u_T(r = 0.12), \Lambda'/\Lambda'_{rms})$  for our run R7. The contours and the shading are for the logarithms of the joint PDFs.

- [15] W. E and J.-G. Liu, J. Comp. Phys. **124**, 368 (1996).  
 [16] H. Clercx, G. Heijst, D. Molenaar, and M. Wells, Dyn. Atmos. Oceans **40**, 3 (2005); G.J.F. van Hei-

- jst, H.J.H. Clercx, and D. Molenaar, J. Fluid. Mech. **554**, 411 (2006).  
 [17] Y.-K. Tsang, E. Ott, T.M. Antonsen, and P.N. Guzdar, Phys. Rev. E **71**, 066313 (2005).  
 [18] G. Boffetta, J. Fluid Mech. **589**, 253 (2007).  
 [19] M.M. Bandi and C. Connaughton, Phys. Rev. E **77**, 036318 (2008).  
 [20] Experiments [5, 6, 7] achieve homogeneity via a periodic, square-wave forcing with amplitude  $F_0$ ; this introduces another time-scale in the problem; to avoid this complication we work with a time-independent force.  
 [21] We employ ESS since forward-cascade inertial ranges have a very modest extent even in the largest DNS studies [17, 18] that use periodic domains and hyperviscosity.